ROYAL SOCIETY
OF CHEMISTRY

PAPER

Check for updates

Elucidating the degradation mechanisms of Pt-free anode anion-exchange membrane fuel cells after durability testing†

John C. Douglin, [iD] [a] Ramesh K. Singh, [iD] [ab] Ami C. Yang-Neyerlin, [c] Cheng He, [c] Karam Yassin, [ad] Hamish A. Miller, [iD] [e] Maria V. Pagliaro, [e] Laura Capozzoli, [e] Enrique Carbo-Argibay, [iD] [f] Simon Brandon, [ad] Paulo J. Ferreira, [fgh] Bryan S. Pivovar*[c] and Dario R. Dekel [iD] *[ad]

The development of anion-exchange membrane fuel cells (AEMFCs) has recently accelerated due to synergistic improvements yielding highly conductive membranes, stable ionomers, and enhanced alkaline electrocatalysts. However, cell durability, especially under realistic conditions, still poses a major challenge. Herein, we employ low-loadings of Pt-free Pd-based catalysts in the anode of AEMFCs and elucidate potential degradation mechanisms impacting long-term performance under conditions analogous to the real-world (high current density, H_2–air (albeit CO_2-free), and intermittent operation). Our high-performing AEMFCs achieve impressive performance with power densities approaching 1 W cm^{-2} and current densities up to 3.5 A cm^{-2}. Over a 200 h period of continuous operation in H_2–air at a current density of 600 mA cm^{-2}, our model Pd/C–CeO_2 anode cell exhibits record stability (~30 μV h^{-1} degradation) compared to the literature and up to 6× better stability than our Pd/C and commercial Pt/C anode cells. Following an 8 h shutdown, the Pd/C–CeO_2 anode cell was restarted and continued for an additional 300 h with a higher degradation rate of ~600 μV h^{-1}. Thorough *in situ* evaluations and post-stability analyses provide insights into potential degradation mechanisms to be expected during extended operation under more realistic conditions and provide mitigation strategies to enable the widespread development of highly durable AEMFCs.

1. Introduction

The use of hydrogen as an alternative fuel has numerous benefits including, but not limited to: availability to both energy-poor and energy-rich countries since it can be produced from water, the versatility to be manufactured from domestic energy resources, and the practicality of being both a high-efficiency energy storage medium and transport medium.[1,2] In light of this, since polymer electrolyte fuel cells powered by hydrogen have been targeted as an alternate solution for the transportation industry, major infrastructure investments from automobile companies and governments have been announced[3,4] and implemented[5,6] to complement the growth and advancement of the technology.

The incumbent fuel cell technology for the transportation sector is the proton exchange membrane fuel cell (PEMFC). Owing to the acidic operating environment, the use of scarce platinum-based electrocatalysts in both electrodes has erected a formidable barrier to attaining the U.S. Department of Energy stack cost target of 30 \$ kW_{net}^{-1} and has thus hindered its large-scale adoption to date.[4,7–9] Despite this existential challenge, since the first high-power publication one decade ago,[10] anion-exchange membrane fuel cell (AEMFC) technology has made incredible progress in recent years owing to the switch to an alkaline operating environment, positioning it as a viable contender to the mature PEMFC.[11,12] Some of the technology's notable achievements include highly conductive anion-exchange membranes (AEMs),[13–18] efficient hydrogen oxidation reaction (HOR) catalysts,[19–29] membrane electrode assembly

[a]The Wolfson Department of Chemical Engineering, Technion – Israel Institute of Technology, Haifa 3200003, Israel. E-mail: dario@technion.ac.il

[b]CO₂ Research and Green Technologies Centre, Vellore Institute of Technology (VIT), Vellore 632014, Tamil Nadu, India

[c]Chemistry and Nanoscience Center, National Renewable Energy Laboratory (NREL), Golden, CO, 80401, USA. E-mail: bryan.pivovar@nrel.gov

[d]The Nancy & Stephen Grand Technion Energy Program (GTEP), Technion – Israel Institute of Technology, Haifa 3200003, Israel

[e]Istituto di Chimica Dei Composti Organometallici (CNR-ICCOM), Via Madonna Del Piano 10, Sesto Fiorentino, 50019 Firenze, Italy

[f]International Iberian Nanotechnology Laboratory (INL), Av. Mestre José Veiga s/n, 4715-330, Braga, Portugal

[g]Mechanical Engineering Department and IDMEC, Instituto Superior Técnico, University of Lisbon, Av. Rovisco Pais, 1049-001 Lisboa, Portugal

[h]Materials Science and Engineering Program, The University of Texas at Austin, Austin, Texas 78712, USA

† Electronic supplementary information (ESI) available. See DOI: https://doi.org/10.1039/d3ta07065d

This journal is © The Royal Society of Chemistry 2024

J. Mater. Chem. A, 2024, **12**, 10435–10448 | **10435**

(MEA) optimization,[30–33] and platinum group metal (PGM)-free oxygen reduction reaction catalysts.[34–36] The latter achievement positions AEMFC technology to eventually attain the vehicular stack cost target.[9]

The main challenge of this technology however, is cell durability, and on this front, only limited studies report on membrane[16,37] and cell stability.[16,30,31,38–40] Furthermore, the majority of cell durability reports in the literature primarily use pure oxygen (>99% O_2) on the cathode, rely on Pt-based catalysts in both electrodes and are represented as continuous data plots under a constant current density or constant voltage operating mode without any interruptions or shutdown/restart cycles. During operation at a steady state, performance may wain over time due to issues such as flooding, dehydration, carbonation and other phenomena occurring within the fuel cell. These performance losses can sometimes be reversed by employing certain techniques that are commonly seen in the AEMFC literature such as adjusting the fuel and oxidant dewpoint temperatures, tuning their flow rates and performing periodic polarization curves to re-adjust the water levels within the cell. Alternatively, AEMFCs suffer irreversible losses as a result of the persistent degradation of essential cell components over time.[14,38]

To the best of our knowledge, there are only a few reports in the literature on H_2-AEMFCs utilizing CO_2-free air with Pt-based anodes and even less using ambient air. For example, one group reported on AEMFC stability for 125 h with a voltage degradation rate of 633 $\mu V\ h^{-1}$ for the first 90 h using a PtRu/C anode.[41] Likewise, another group showed durability for a radiation-grafted high-density polyethylene-based AEM operated for 440 h in AEMFCs with a degradation rate of $68 \pm 1\ \mu V\ h^{-1}$ using a Pt/C anode.[17] Similarly, some researchers displayed AEMFC durability for 1000 h at 600 mA cm^{-2} with a low voltage degradation rate of 32 $\mu V\ h^{-1}$ using a PtRu/C anode.[31] However, these and other reports[14,16,41,42] were operated continuously and do not give deep insights into the associated degradation mechanisms after protracted cell operation.

Advancing AEMFCs toward commercial deployment as competitive energy conversion devices in the transportation industry, requires a focused effort on understanding the irreversible degradation mechanisms while operating with air in the cathode and selecting robust and proven alternatives to Pt-based catalysts.[38] In addition, since vehicles are operated intermittently, it is important to elucidate the impact of shutdown/restart cycles on long-term fuel cell activity and performance.

Given the necessity of identifying the underlying variables required to improve MEA resilience, we first aimed to curtail any adverse effects on cell durability due to the HOR at the anode with a Pt alternative as PGM materials show the highest activity in catalyzing the HOR in AEMFCs.[43,44] To that purpose, we selected a model, cost-neutral (relative to Pt) Pd/C–CeO$_2$ (10 wt% Pd) catalyst as our Pt-free anode, as Pt is extensively researched in the literature. The composite oxophilic ceria on carbon (C–CeO$_2$) support, which has been methodically investigated in our previous work,[27,45] assists in providing sites for OH_{ad}, where H is adsorbed onto the Pd surface. This

bifunctional mechanism leads to an overall increase in the efficiency of the HOR process.[26,46–48] An example by Singh et al.,[27] demonstrates the effective quantification of the Pd–CeO$_x$ interfacial area as the major contributor to the oxophilic effect of CeO$_x$ on Pd. This interfacial area was correlated with improved HOR performance observed in both rotating disk electrode (RDE) and AEMFC tests. Speck et al.,[49] investigated the dissolution behavior of Pt and Pd covered with atomic layer deposited CeO$_x$ layers known as "buried interfaces" by using online inductively-coupled plasma-mass spectroscopy (ICP-MS) and showed a significant decrease in the dissolution rate ($\times 15$ times lower) of Pd covered with 20-CeO$_x$ layers.

Other noteworthy advancements have been achieved in the design of these types of catalysts by engineering the Pd–CeO$_2$ interface through a variety of synthetic methods such as wet chemical,[26,29,45] reactive spray deposition technology,[46] controlled surface reactions,[27] and atomic layer deposition.[49] Though significant progress has been made in the design of Pd/C–CeO$_2$ catalysts, their stability in AEMFCs is not well studied and limited to the work by Omasta et al.,[39] where investigations into the short-term stability of the catalyst in H_2–O_2 mode were made for 100 h resulting in a severe voltage degradation rate of 2500 $\mu V\ h^{-1}$.

In this article, we initially demonstrate that our AEMFCs with Pd-based anodes exhibit good polarization performance i.e., power densities approaching 1 W cm^{-2} and current densities up to 3.5 A cm^{-2} with H_2–O_2. We next test the stability of the Pd/C–CeO$_2$ and Pd/C anode-based AEMFCs in H_2–air under a constant current density of 600 mA cm^{-2} for 500 h until irreversible performance degradation is realized in both cells. Our Pd/C–CeO$_2$ anode cell shows a significantly low voltage degradation rate of 30 $\mu V\ h^{-1}$ (after the first 200 h) compared to a Pd/C anode cell (100 $\mu V\ h^{-1}$) and a commercial Pt/C anode cell (190 $\mu V\ h^{-1}$). Around the 200 h mark, the Pd/C–CeO$_2$ anode cell experienced a complete shutdown for an 8 h period due to a power outage. After the power resumed, the cell was returned to the same pre-shutdown operating conditions and the durability test resumed for an additional 300 h. The post-shut-down degradation rate accelerated to 600 $\mu V\ h^{-1}$ (last 300 h) and could not be reversed by any previously mentioned performance recovery techniques. The retrieved Pd/C–CeO$_2$ anode membrane electrode assembly (MEA) was thoroughly analyzed before and after durability testing using scanning electron microscopy (SEM) uncovering changes in the electrode structures, morphology, and composition. Our analysis confirms the significant electrochemical dissolution of cathode Pt and its transport through the AEM with eventual redeposition on the CeO$_2$ regions of the anode layer. Additional sources are identified as increased overpotential in the mass-transport region and chemical degradation of the ionomer and membrane on the cathode side.

2. Experimental

2.1 Materials

Deionized (DI) water with a purity of 18.2 MΩ cm, hydrogen with purity of 99.999% and CO_2-free air (21% O_2), referred to

10436 | J. Mater. Chem. A, 2024, 12, 10435–10448

This journal is © The Royal Society of Chemistry 2024

throughout the manuscript as air, were used. Carbon black (Vulcan XC-72) was purchased from Cabot Corp., USA. The gas diffusion layer (GDL) was Toray TGP-H-060 with 5% PTFE wet-proofing. Pt/C was purchased from Alfa Aesar (40 wt% Pt, 60 wt% carbon, HiSPEC 4000). All metal salts and reagents were purchased from Sigma-Aldrich and used as received. All aqueous solutions were freshly prepared with DI water.

2.2 Catalyst synthesis

2.2.1 Pd/C–CeO$_2$.
The Pd/C–CeO$_2$ was synthesized in a manner similar to our previous work.[26] Vulcan XC-72 (4 g) was added to a solution of Ce(NO$_3$)$_3$·6H$_2$O (10.1 g) in H$_2$O (250 mL). The mixture was kept under stirring for 60 min and then sonicated for 30 min. After adjusting the pH to 12 with KOH, the resulting suspension was stirred for 2 h. The product was separated by filtration and washed with H$_2$O until a neutral pH was obtained. The product was dried at 65 °C, then subsequently heated under air in a tube furnace at 250 °C for 2 h. Cooling to room temperature was conducted under a flow of Ar. The total yield of C–CeO$_2$ was 7.15 g with C and CeO$_2$ wt% of 56 and 44%, respectively.

C–CeO$_2$ (4 g) was suspended in water (500 mL), stirred vigorously for 30 min and sonicated for 20 min. To this mixture, a solution of K$_2$PdCl$_4$ (1.38 g) in water (60 mL) was slowly added (during ca. 1 h) under vigorous stirring, followed by the addition of an aqueous solution of 2.5 M KOH (8.4 mL). Next, ethanol (50 mL) was added, and the resulting mixture was heated at 80 °C for 60 min. The desired product Pd/C–CeO$_2$ was filtered off, washed several times with distilled water to neutrality and finally dried under vacuum at 65 °C until a constant weight was reached. The yield of Pd/C–CeO$_2$ was 4.45 g.

2.2.2 Pd/C.
Vulcan XC-72 (6.0 g) was suspended in 250 mL of ethylene glycol and sonicated for 20 min in a 500 mL three-neck round-bottomed flask. Then a solution of 1.0 g of PdCl$_2$ in a mixture of H$_2$O (50 mL), ethylene glycol (50 mL) and 6 mL HCl (37%) was added dropwise under stirring in an N$_2$ stream. After adequate stirring, an alkaline solution of NaOH (5 g) in H$_2$O (10 mL) and ethylene glycol (35 mL) was introduced in the reactor, which then was heated at 125 °C for 3 h under an N$_2$ atmosphere. Then the mixture was cooled to room temperature. The solid product was filtered off and washed with H$_2$O to neutral pH. The final product was dried in a vacuum oven at 40 °C (yield: 6.53 g).

2.2.3 Instrumentation.
Scanning electron microscopy (SEM), scanning transmission electron microscopy (STEM), and energy dispersive X-ray spectroscopy (EDX) sample characterization were performed using a TESCAN Gaia 3 Focused Ion Beam (FIB)/SEM. The microscope hosts a 30 kV Triglav electron column and a Cobra Focused Gallium Ion Beam column. SEM images of the electrode surfaces were acquired using the two in-beam Secondary Electron (SE) and Back Scattered Electron (BSE) detectors, located inside the electron column. Transmission electron microscopy (TEM) was performed on a Philips CM12 microscope at an accelerating voltage of 100 kV. Z-contrast STEM analysis using TEM was performed on a JEOL JEM-F200 instrument. High-angle annular dark field (HAADF) images were recorded using FEI Titan Cubed Themis operated at 200 kV.

2.3 Anion exchange membrane fuel cell fabrication and testing

2.3.1 Membrane and ionomer preparation.
Sulfonamide-linked alkyl ammonium perfluorinated anion exchange membrane (PF AEM) Gen 2 polymer was used as both membrane and ionomer material to fabricate membrane electrode assemblies (MEAs) for fuel cell testing. The detailed synthesis and characterization of PF AEM were reported previously.[50,51]

2.3.2 Membrane electrode assembly fabrication.
Solid PF AEM ionomer was applied during the MEA fabrication. The solid ionomer was ground for 10 minutes to reduce the size of the big particles. Platinum on Vulcan carbon catalyst, solid PF-AEM ionomer, DI water, and 2-propanol were mixed to yield a final ink with 0.4 ionomer/carbon (I/C) ratio and 1 mg mL^{-1} Pt concentration. Then the catalyst mixture was sonicated for 20 minutes in an ice bath. The MEA was fabricated by hand spraying catalyst ink onto a gas diffusion layer and had 0.55 ± 0.05 mg$_{Pt}$ cm^{-2} Pt loading for the cathodes. The anodes with Pd/C–CeO$_2$, Pd/C and Pt/C catalysts were fabricated using the abovementioned method, and their PGM loadings were 0.30 ± 0.10 mg$_{PGM}$ cm^{-2}.

2.3.3 Fuel cell testing.
Before assembling an MEA for fuel cell testing, two GDEs and a PF AEM Gen 2 membrane were soaked in 1 M KOH solution for at least 60 min (total) with the replacement of a new base solution every 20 minutes to ensure full exchange to OH$^-$ form. The membrane was sandwiched between two gas diffusion electrodes (GDEs) and pressed together between two single-pass serpentine flow graphite plates using fiber-reinforced PTFE gaskets to obtain a 25% compression. The MEA was secured in a 5 cm^2 Fuel Cell Technologies hardware with a torque of incremental steps of 4.5 N m.

The assembled fuel cell was attached to an 890E Scribner Fuel Cell Test Station. The cell temperature, anode and cathode dew points were set at 60 °C initially (100% relative humidity). H$_2$ and N$_2$ were pumped through the anode and cathode, respectively, at 1.0 standard liter per minute (slpm) until the desired temperatures were achieved and stabilized. Then the N$_2$ was switched to O$_2$ and an absolute pressure of 121 kPa was applied to both electrodes. After the open circuit voltage (OCV) stabilized, a constant voltage of 0.5 V was applied ultimately achieving a constant current density after 40–50 minutes. Polarization curves were acquired by sweeping the voltage from OCV to 0.1 V at a scan rate of 10 mV s^{-1} at various relative humidity (RH) conditions. Additional polarization curves were acquired after switching the cathode from O$_2$ to air and again after increasing the cell temperature to 70 °C. The fuel cell durability testing was recorded at a constant current density of 600 mA cm^{-2} under H$_2$–air at cell temperatures of both 60 and 70 °C at 100% RH and backpressures as indicated in the figures described in Section 3 below.

2.3.4 Electrochemical impedance spectroscopy (EIS).
EIS was measured using a Solartron 1260 frequency response analyzer under H$_2$ and N$_2$ for the anode and cathode, respectively pumped at 1.0 slpm. A cell temperature was set at 70 °C

This journal is © The Royal Society of Chemistry 2024

J. Mater. Chem. A, 2024, 12, 10435–10448 | 10437

(100% relative humidity) with a total pressure of 131 kPa at a cell potential of 0.45 V *vs.* standard hydrogen electrode (SHE) over a frequency ranging from 10 000 to 0.1 Hz.

2.4 Voltage degradation calculations

In the literature, various methods can be found to calculate degradation rates of AEMFCs during durability studies. For instance, the difference in the voltage values at the start and end can be divided by the duration of the experiment.[52] While this may be a straightforward way, we do not believe that it presents the most accurate depiction of voltage degradation, given that various techniques may be employed to recover the voltage or reduce the high-frequency resistance (HFR) over time. To mitigate any biases, we took our raw Excel dataset containing the time and voltage values for the 500 h durability plots[53] and superimposed straight lines between the start and end voltage values. Then we derived the equations of each straight line ($y = mx + c$) directly in Microsoft Excel. We then applied the straight-line equations beginning at the voltage value corresponding to the first-time value, by substituting the first-time value for x in the equation. The remaining time values were substituted for the remaining time values in the dataset in order to obtain a depiction of the straight-line degradation plots of each of our durability experiments.

2.5 1D AEMFC model simulation

To further probe the performance stability of our cell with a Pd/C–CeO₂ anode, we used a 1D AEMFC model developed by our group.[54,55] The computational domain consists of a 5-layer MEA consisting of a membrane, anode and cathode catalyst layers (CLs), and anode and cathode GDLs. The model considers multiple phenomena, including gas, water and ion transport as well as the electrochemical reactions in the CLs; hydrogen oxidation reaction in the anode and oxygen reduction reaction in the cathode. Additionally, we incorporate the degradation kinetics of the ionomeric materials in the membrane and the anode and cathode CLs. By considering all these factors, our model provides comprehensive insight into the changes occurring in the cell over time.

The primary dependent variables in our model include the molar concentrations of hydrogen, oxygen, nitrogen, and water, as well as molar velocities, partial pressures, and electric fields. The water appears in three forms: liquid, vapor, and within the ionomer. The liquid water in the CL impacts the porosity available for gas transport. Water transport through the membrane is modeled as a combination of diffusion and electro-osmotic drag, while transport through the GDL is single-phase and modeled using a Maxwell–Stefan approach with Darcy's law. The electrochemical reactions are modeled using Butler–Volmer kinetics to realize the kinetics of the hydrogen oxidation reaction in the anode and the oxygen reduction reaction in the cathode.

3. Results and discussion

3.1 AEMFCs performance and durability

Fig. 1 portrays polarization curves of the Pd/C–CeO₂ anode AEMFC operated at 70 °C and various dewpoints in H₂–O₂ (Fig. 1A) and H₂–air (Fig. 1B) modes, while ESI Fig. 1† displays the corresponding Pd/C anode AEMFC. In H₂–O₂ mode, the Pd/C–CeO₂ anode AEMFC outperforms the Pd/C anode AEMFC both in terms of peak power density and limiting current density, irrespective of the dewpoint setting. Further details of the AEMFC performance of the Pd/C–CeO₂ anode AEMFC are given in ESI Table 1.† A ∼30 mV higher OCV is observed with H₂–O₂ as compared to H₂–air at all dew point settings. Furthermore, in the higher voltage, lower current density
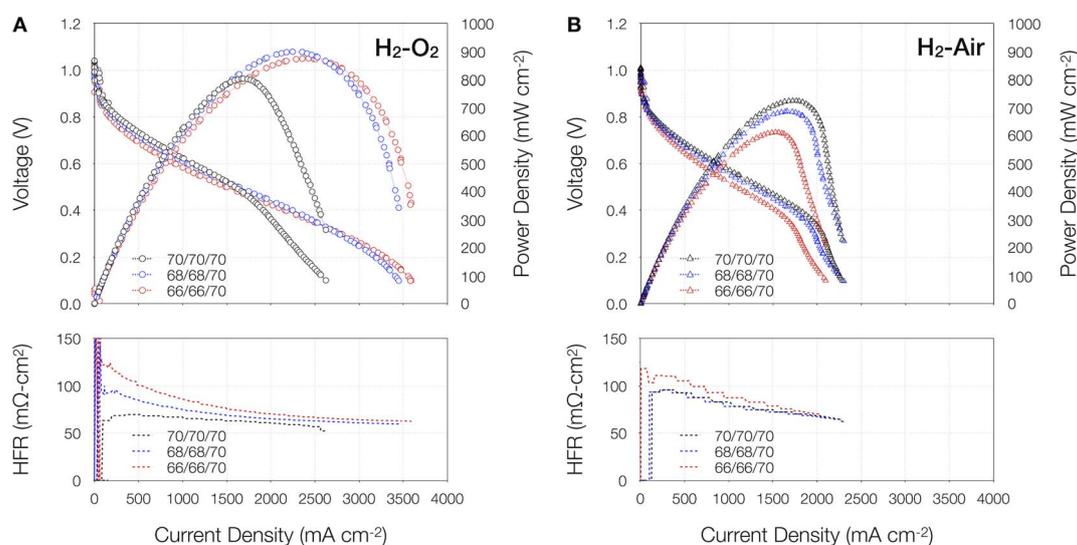

Fig. 1 *i–P* and *i–V* curves of (A) H₂–O₂ and (B) H₂–air AEMFCs with Pd/C–CeO₂ anode and Pt/C cathode and their respective area specific resistance (ASR) plots shown in the lower panels. The cells were operated at 70 °C with varying anode and cathode dew points. H₂–O₂ and H₂–air flow rates were 1|1 slpm, with a back pressure of 131 kPa. Further specifics about the MEAs can be found in the Experimental section. The figure legends indicate anode dew point/cathode dew point/cell temperature. Horizontal gridlines in all figures correspond to the left *y*-axis.

10438 | *J. Mater. Chem. A*, 2024, **12**, 10435–10448

This journal is © The Royal Society of Chemistry 2024

regions of the i–V curves, the voltage efficiencies, notably at 0.8 and 0.6 V decline consistently with a reduction in the dew point settings, regardless of the cathode oxidant. However, with H_2–O_2, at voltages $\leq$ 0.4, the fully humidified condition (70/70/70) appears to impede the higher current density mass transport region on the Pd/C–CeO$_2$ anode AEMFC, given that the optimized operating conditions (66/66/70 and 68/68/70) both arrive at performances as high as ~900 mW cm^{-2} and ~3500 mA cm^{-2}. Additionally, the observed H_2–O_2 current density at 0.65 V of our Pd/C–CeO$_2$ anode AEMFC reaches 900 mA cm^{-2} which is close to the U.S. Department of Energy 2022 target (1000 mA cm^{-2}).[56]

By contrast, the Pd/C anode AEMFC (ESI Fig. 1A†), follows a similar trend to the Pd/C–CeO$_2$ anode cell in the higher voltage region, with the exception of the 68/68/70 setpoint yielding slightly higher performance than the 70/70/70 setpoint at both 0.8 and 0.6 V. At lower voltages, the Pd/C anode cell seems to be a bit more sensitive to dehydration in the higher current density region as the 68/68/70 operating condition yields the highest performance, 550 mW cm^{-2} (peak power density) and 2050 mA cm^{-2} (limiting current density), followed by the 70/70/70 settings. At the 66/66/70 operating condition, the peak power and limiting current density values fell to 478 mW cm^{-2} and 1588 mA cm^{-2}, respectively.

In H_2–air mode, the Pd/C–CeO$_2$ anode AEMFC (Fig. 1B) again performed better than the Pd/C anode cell (ESI Fig. 1B†), however this time, both AEMFCs were more sensitive to water content, with the best performance achieved in completely humidified conditions. Nevertheless, regardless of the setpoints, both cells experienced mass-transport issues, as shown by the inflections of the i–V curves at ~0.4 V. This decrease may be associated with mass-transport limitations due to the presence of N_2 and reduced partial pressure of O_2. The literature has shown that further optimization of the electrodes and operating conditions, such as increasing the hydrophobicity of the anode by adding PTFE to the catalyst layer, adjusting ionomer content, adding microporous layers and setting the anode dew point to be slightly lower than the cathode anode can improve mass transport performance.[30,57,58]

The HFR plots give more insight into cell hydration and water dynamics. As seen in the lower panels of Fig. 1 and ESI Fig. 1,† the HFR values are higher $i.e.$ >100 mΩ cm^2 at the lowest dew point settings (66/66/70), regardless of anode type. In all cases, the HFR values decrease as current density increases indicating similarities in membrane hydration and water dynamics. The 70/70/70 and 68/68/70 dew point settings displayed similar HFR trends during the acquisition of the polarization curves in H_2–air mode for both anode types. Hence, we adopted the 70/70/70 dew point values for the 500 h durability experiments discussed later in the manuscript.

The beginning of life (BOL) polarization curves in H_2–air for the AEMFCs with Pd/C–CeO$_2$ and Pd/C anodes are shown in (Fig. 2A and B). As expected, the Pd/C–CeO$_2$ anode exhibits improved cell performance due to the increased operating temperature from 60 to 70 °C and in comparison to the Pd/C anode cell, which confirms previous reports.[26,27,46,49] The improved performance of the Pd/C–CeO$_2$ compared to Pd/C is

attributed to the "bifunctional HOR mechanism" in alkaline electrolytes; namely a decrease in hydrogen binding energy (HBE), and OH$^-$ spillover from CeO$_2$ to Pd, which facilitates the Volmer step and is well-documented in literature.[26,27,59] The summary of the cell performance results is given in ESI Table 2† presenting further insights into the higher voltage efficiencies of the Pd/C–CeO$_2$ anode at 0.8, 0.6 and 0.4 V compared to the Pd/C anode.

To investigate the performance durability of our anodes in H_2–air, we initially recorded the durability data of a Pd/C–CeO$_2$ anode cell for 230 h at a cell temperature of 60 °C (Fig. 2C) under a constant current density load of 600 mA cm^{-2}. As seen from the figure, the cell exhibited good stability with a voltage degradation rate of 80 μV h^{-1} and virtually no increase in the HFR. We compared this to a cell containing a Pt anode tested under the same conditions for 310 h and the Pt anode cell had a higher degradation rate of 190 μV h^{-1} (ESI Fig. 2†). This encouraged us to extend the operation time of our Pd/C–CeO$_2$ durability as well as compare the enhancement afforded by Ceria to the Pd. Consequently, we performed an additional durability test in H_2–air on a fresh Pd/C–CeO$_2$ anode as well as a Pd/C anode cell for 500 h at a cell temperature of 70 °C under the same constant current density load of 600 mA cm^{-2}.

As seen from Fig. 2D, for the first ~200 h, the Pd/C–CeO$_2$ cell had a lower voltage degradation rate of 30 μV h^{-1}, which is a bit counterintuitive as it would be anticipated that an increase in the cell temperature would accelerate the membrane and cathode ionomer degradation.[38] We therefore attribute the ~2.5 times higher stability to the increased operating temperature which has also shown in the literature via theoretical simulations to provide higher stability due to the rise in the reaction kinetics leading to an increase in the amount of back-diffused water molecules from the anode to the cathode to improve the efficacy of the oxygen reduction reaction.[60] The initial Pd/C–CeO$_2$ degradation rate (until ~200 h) is compared with the published results operated with H_2–air (Table 1) using platinum group metal (PGM)-catalysts in the anode showing it to be the only Pd/C–CeO$_2$ anode work operated in H_2–air with the lowest reported degradation rate on a Pt-free anode catalyst, which is highly encouraging for long-lasting AEMFCs. Furthermore, our 1D model predicts that the cell would have continued with a relatively stable cell performance up to 500 h.

It is worthwhile mentioning that the durability studies in the literature are primarily based on anodes containing Pt which has an order of magnitude lower dissolution rate than Pd-based catalysts.[49] Nevertheless, we were able to achieve a significantly lower degradation rate mainly due to the dissolution stability of Pd/C–CeO$_2$ provided by CeO$_2$.[45,49]

Following the initially higher stability of the Pd/C–CeO$_2$ anode cell at 70 °C for approximately the same duration as the 60 °C cell, the system encountered a shutdown due to a power outage for 8 h, and all temperature controls were turned off, backpressure was released, and fuel flow stopped. The MEA remained within the cell hardware at room temperature during the shutdown period, and all input and output connections remained attached. After the power returned, the system was restarted and returned to the settings before the shutdown at
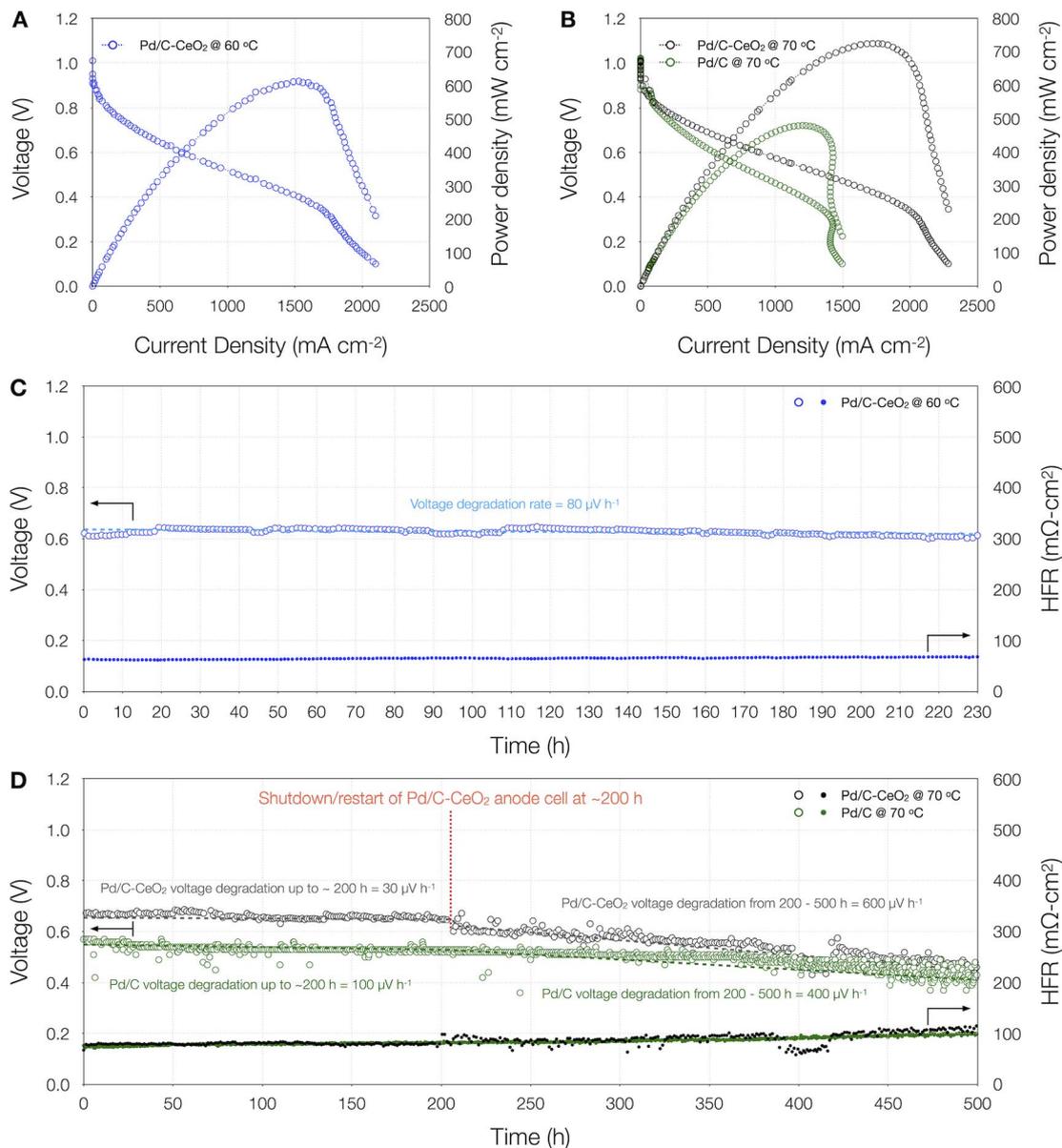
This journal is © The Royal Society of Chemistry 2024

J. Mater. Chem. A, 2024, **12**, 10435–10448 | **10439**

Fig. 2 Beginning of life polarization curves of AEMFCs with (A) a Pd/C–CeO$_2$ anode at 60 °C and, (B) Pd/C–CeO$_2$ and Pd/C anodes at 70 °C. Cell durability experiments of AEMFCs with (C) a Pd/C–CeO$_2$ anode at 60 °C for 230 h and, (D) Pd/C–CeO$_2$ and Pd/C anodes at 70 °C for 500 h each. All tests were performed in H$_2$–air with flow rates of 1|1 slpm. Further specifics about the MEAs can be found in the Experimental section. The 60 °C polarization curves were performed with backpressure of 121 kPa on both sides. The 70 °C polarization curves and durability experiments were conducted with back pressure of 131 kPa on both sides and at current density load of 600 mA cm^{-2}, respectively. The dashed lines through the voltage plots in (C) and (D) depict the straight-line degradation based on an algorithm that was used to calculate the voltage degradation rates listed on the plots in units of μV h^{-1}. Horizontal gridlines in all figures correspond to the left y-axis. Further details on the voltage degradation algorithm can be found in Experimental section 2.4 and ESI Fig. 3.†

70 °C and a constant current density of 600 mAcm^{-2} for another 300 h.

Fig. 2D and ESI Fig. 3B† show that during the 200–500 h operation timeframe, a higher degradation rate of 600 μV h^{-1} is observed for the Pd/C–CeO$_2$ anode cell compared to 400 μV h^{-1} in the case of the Pd/C anode cell which operated continuously without any shutdown.

ESI Fig. 4A† shows a comparison between the model prediction and the experimental data, solely relying on the

design and operating parameters derived from the experimental measurements without fitting parameters. The model depicts excellent agreement between the predicted and experimental data up to cell shutdown (~200 h). Our modeling results demonstrate that the cell would have continued with a relatively stable cell performance up to 500 h of operation, confirming that the voltage decay rate in the experimental data up to the 200 h point (30 μV h^{-1}) would have continued until 500 h in the event that the shutdown had not occurred. This is further

10440 | J. Mater. Chem. A, 2024, **12**, 10435–10448

This journal is © The Royal Society of Chemistry 2024

Table 1 Comparison of the voltage degradation rates of AEMFCs with platinum group metal (PGM)-catalysts in the anode operated with H_2–air reported in the literature

Anode	PGM loading (mg_{PGM} cm^{-2})	Current load (mA cm^{-2})	Cell temperature (°C)	Time (h)	Voltage degradation rate (μV h^{-1})	Ref.
Pd/C–CeO₂	0.33	600	70	200	30[a]	This work
Pt/C	0.40	200	80	125	~240	41
PtRu/C	0.99	600	80	550	~220	14
Pt/C	<0.15	500	95	300	~330	16
PtRu/C	0.70	600	80	100	~200	42
Pt/C	0.60	600	70	440	68	17
PtRu/C	0.70	600	65	1000	32	31

[a] For the first 200 h.

supported by the ion exchange capacity (IEC) profiles shown in ESI Fig. 4B† which shows a decrease in IEC in both the cathode catalyst layer as well as the side of the membrane closest to the cathode as time goes by. Consistent with our previous results,[54] the reduction in the performance stability is caused by the ionomer degradation at the membrane | cathode interface as well as within the membrane. These modeling results show that chemical ionomer degradation is an important mechanism contributing to cell performance loss.

In order to gain further insight into the behavior of the cell over time, periodic polarization curves were obtained at the 96th, 192nd, 288th, 384th, 480th, and 500th h of operation for both cells throughout the their 500 h durability experiments depicted in Fig. 2D. These were deconvoluted into their respective kinetic, ohmic and mass-transport contributions following the methods reported in the literature.[32,39,61] ESI Fig. 5† shows the polarization curves at the specified times for the Pd/C–CeO₂ and Pd/C anode cells, respectively, which indicate significant changes in the mass-transport overpotential regions of both cells. A closer look at the Pd/C–CeO₂ anode cell reveals a decrease in limiting current density from 1813 to 1427 mA cm^{-2} from the 192nd to the 288th h (Fig. 3C), signifying an increase in mass-transport overpotential, while a slight decrease is seen in the kinetic overpotential (Fig. 3A) and no change in the ohmic overpotential (Fig. 3B). The subsequent polarization curve at the 384th h reveals further increases in kinetic (Fig. 3A), ohmic (Fig. 3B) and mass-transport (Fig. 3C) overpotentials.

For the Pd/C anode cell, a similar increase in mass-transport overpotential is only seen at the 384th h polarization curve represented by a decrease in the limiting current density (ESI Fig. 6C†), while the kinetic (ESI Fig. 6A†) and ohmic (ESI Fig. 6B†) overpotentials changes are more subtle. The increase in mass-transport overpotential during the 384th h polarization curve corresponds to an increase in HFR during the durability experiment as seen in Fig. 2D. The sudden decrease in durability performance after the 288th h polarization curve of the Pd/CeO₂ anode cell suggests that the shutdown event at ~200 h played a huge factor. Interestingly, since the Pd/C anode cell displayed a comparable decline in durability performance after the 384th h polarization curve, it implies that both cells experienced irreversible voltage deterioration.[38]

3.2 Electrochemical impedance spectroscopy diagnostics of the MEAs

Electrochemical impedance spectroscopy diagnostic tests were also carried out for both Pd/C–CeO₂ and Pd/C anode cells to shed light on the degradation mechanisms (Fig. 4). The Nyquist plots show the typical shape of the transmission line network with no Faradaic process similar to that reported by Setzler and Fuller for PEMFCs.[62] The high-frequency intercept is mainly due to the membrane, electronic, and contact resistances.[62–64] The summary of the impedance results is given in ESI Table 3† and as can be seen, the HFR value at the EOL for the Pd/C–CeO₂ anode cell (Fig. 4A) showed a 2.8× increase from the BOL value.
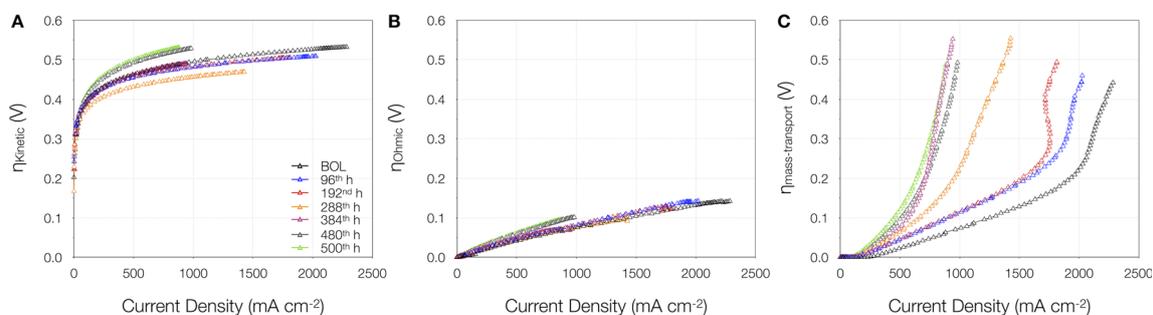

Fig. 3 (A) The deconvoluted *i–V* curves of the Pd/C–CeO₂ anode AEMFC operated in H_2–air at 70 °C recorded during the respective durability tests shown in Fig. 2C at the beginning of life (BOL), 96th, 192nd, 288th, 384th, 480th, and 500th h. (A) Kinetic overpotential, (B) ohmic overpotential and, (C) mass-transport overpotential.
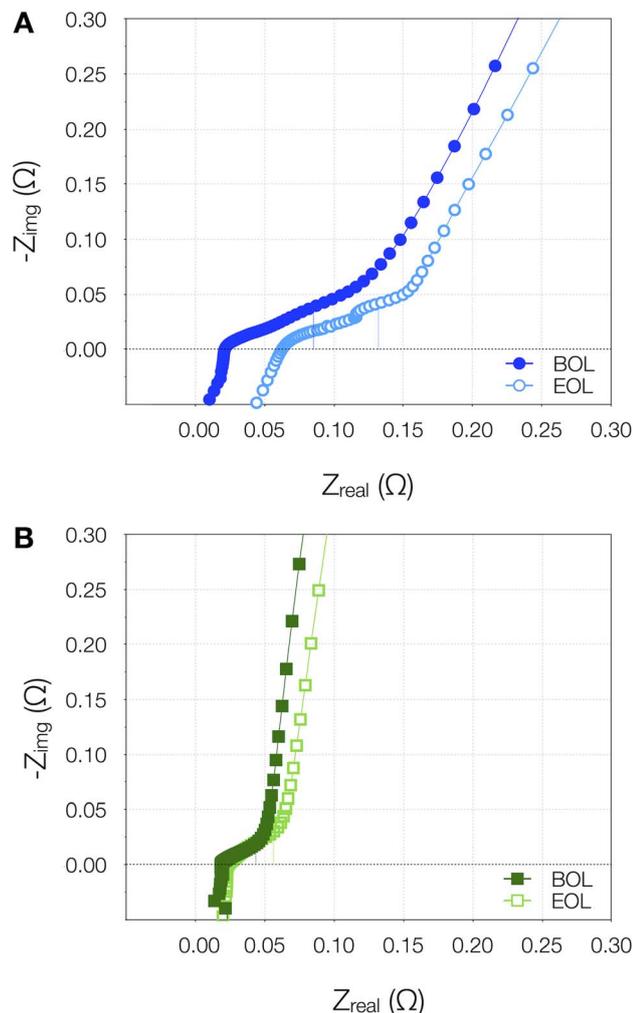
This journal is © The Royal Society of Chemistry 2024

J. Mater. Chem. A, 2024, **12**, 10435–10448 | **10441**

Fig. 4 H_2-N_2 *in situ* EIS diagnostic for (A) Pd/C–CeO$_2$ and, (B) Pd/C anodes at the beginning of life (BOL) and after durability testing at the end of life (EOL).

By comparison, the HFR for the Pd/C anode cell (Fig. 4B) increased by only 1.27× from BOL to EOL. The higher change in HFR for Pd/C–CeO$_2$ is likely due to the shutdown event and is indicative of a long-term issue. The corresponding BOL and EOL cyclic voltammograms (CVs) of the Pd/C–CeO$_2$ and Pd/C anodes are also shown in ESI Fig. 7† and the Pd/C–CeO$_2$ CV features are similar to that reported in our previous work.[26,45,46] After EOL, the CV changes significantly which we attribute partially to the shutdown and higher Pt-migration. In contrast, Pd shows slight differences in the voltammetric feature after durability testing.

The HFR values derived from electrochemical impedance spectroscopy (EIS) are in close agreement with those obtained from the fuel cell directly. From the low-frequency intercept (45-degree line), the catalyst layer ionomer resistance is estimated, which is equivalent to the HFR and one-third of the catalyst layer ionomer resistance.[62,65] ESI Table 3† also reveals that the catalyst layer ionomer resistance is as much as 3.2× higher for Pd/C–CeO$_2$ when compared to the Pd/C anode at the BOL and this difference can be attributed to the oxide phase of CeO$_2$. The

catalyst layer ionomer resistance increased by factors of 1.1 and 1.4 after durability testing for Pd/C–CeO$_2$ and Pd/C, respectively (ESI Table 3†). The lower increase in the catalyst layer ionomer resistance after the durability test of Pd/C–CeO$_2$ suggests that the anode catalyst layer ionomer resistance is maintained after the end-of-life (EOL) test.

CV and EIS diagnostics of the corresponding cathodes are given in ESI Fig. 8A–D,† respectively. The CVs of Pt/C cathode associated with the Pd/C–CeO$_2$ anode cell (ESI Fig. 8A†) show a greater decrease in the electrochemical active surface area (ECSA) after durability testing compared to Pt/C cathode in the Pd/C anode cell (ESI Fig. 8C†). At the 70 °C cell temperature condition, the Pd/C–CeO$_2$ anode cell exhibited a ~48% change in ECSA from 44.46 to 23.17 m^2 g$_{Pt}^{-1}$ from BOL to EOL, while the Pd/C anode cell changed by ~10% from 43.10 to 38.58 m^2 g$_{Pt}^{-1}$. This is noteworthy to highlight since similar CV and EIS diagnostic tests performed at the 72nd, 96th, 120th and 216th h intervals during the continuous durability test of the Pd/C–CeO$_2$ anode cell at 60 °C revealed that ECSA only decreased slightly over time (ESI Fig. 9A†) and the impedance trend showed very little change in the membrane and catalyst layer resistances (ESI Fig. 9B†). This is a direct indicator that under normal operation without a shutdown, Pt is gradually lost from the cathode, but the shutdown event appears to exacerbate this effect resulting in a larger decrease in the amount of Pt from the cathode. This is further corroborated by the larger increase in the resistance in the case of Pd/C–CeO$_2$ anode cell (ESI Fig. 8B† compared to ESI Fig. 8D†). Therefore, we believe that this may be the reason for the higher degradation rate observed with Pd/C–CeO$_2$ anode from 200–500 h and may be partially ascribed to the shutdown event.

3.3 SEM and elemental mapping of electrode layers before and after durability testing

Prior to AEMFC testing, microscopic images of the Pd/C–CeO$_2$ and Pd/C anodes (ESI Fig. 10 and 11†) show good dispersion of the Pd nanoparticles (NPs) on both C–CeO$_2$ and carbon supports, respectively. As HR-TEM alone is not sufficiently able to differentiate between individual Pd and CeO$_2$ nanoparticles deposited onto the carbon surface, the Pd/C–CeO$_2$ (10 wt% Pd) catalyst nanostructure is studied using high-resolution Z contrast STEM imaging combined with EDX elemental mapping (ESI Fig. 10†). As can be seen from the elemental maps, the Pd and CeO$_2$ nanoparticles (NPs) are intimately clustered together rather than separated. The very high interfacial contact between Pd and CeO$_2$ in this class of catalyst has been shown to enhance the alkaline HOR activity in AEMFCs.[26,46,66] The Pd/C catalyst (also 10 wt% Pd) morphology is shown in ESI Fig. 11.† In this catalyst, the Pd NPs are distributed over the carbon surface and are generally under 10 nm in size.

Given that similar performance degradation phenomena were observed for the Pd/C–CeO$_2$ and Pd/C anode cells (after the 288th and 384th h polarization curves during the durability tests, respectively), the AEMFC based on Pd/C–CeO$_2$ was recovered from the test cell after 500 h and the two electrode
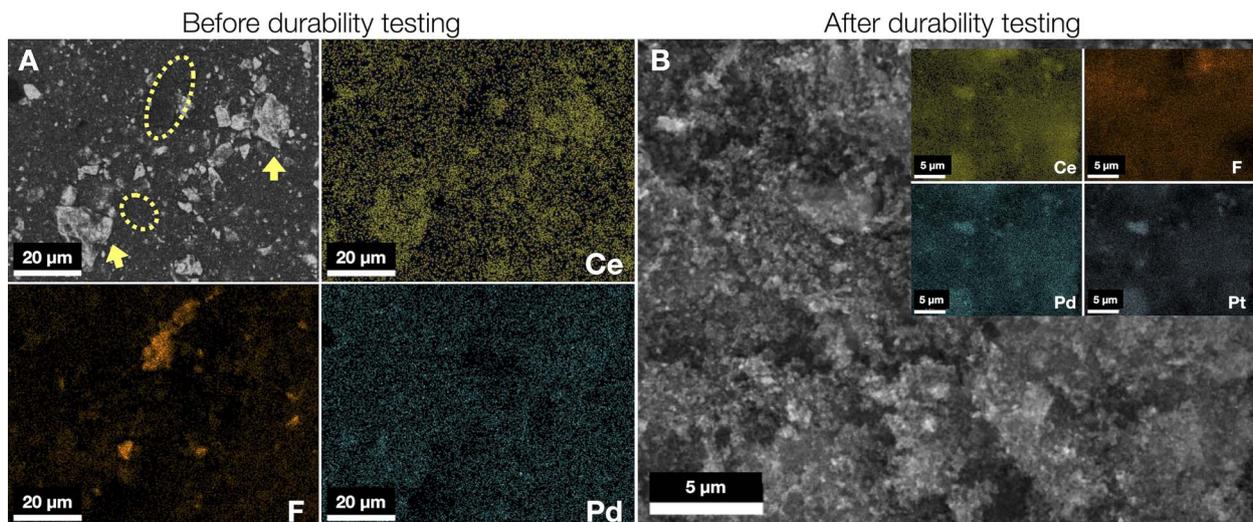
10442 | *J. Mater. Chem. A*, 2024, **12**, 10435–10448

This journal is © The Royal Society of Chemistry 2024

Fig. 5 SEM images and corresponding elemental maps of representative areas of the surface of the Pd/C–CeO$_2$ catalyst layer of the GDE. (A) Before testing SEM image showing Pd/C–CeO$_2$ indicated by yellow arrows and the areas containing the ionomer polymer indicated by yellow ovals as well as elemental maps for Ce, F, and Pd. (B) After the 500 h durability AEMFC test SEM image and elemental maps for Ce, F, Pd and Pt. The scale bar setting of all images in (A) is 20 μm and 5 μm for all images in (B).

layers (anode and cathode) were investigated by SEM and elemental mapping in order to further investigate the Pt loss from the cathode. Sections of the anode and cathode before the operation were also examined to map any significant changes in morphology and elemental distribution of both catalyst layers after 500 h of AEMFC operation. Fig. 5A shows a representative area of the freshly prepared Pd/C–CeO$_2$ anode. Elemental mapping was used to identify the composition of the electrode surface. Distinctive zones covered by Ce and F can be assigned to Pd/C–CeO$_2$ and the ionomer particles (fluorinated polymer backbone), respectively. The electrode surface appears non-homogeneous in nature with catalyst and ionomer particles concentrated in different zones of the surface. The brighter particles indicated by arrows are Pd–CeO$_2$ and the areas containing the ionomer polymer are in yellow ovals.

In Fig. 5B and ESI Fig. 12† (magnified view of Fig. 5B), the recovered Pd/C–CeO$_2$ anode catalyst layer after the 500 h durability test shows magnified portions together with the representative elemental maps for Ce, Pd, and Pt. The images show that the catalyst particles are not agglomerated, but in addition to the presence of Pd and Ce on the catalyst surface, a significant amount of Pt is detected. The only reasonable explanation for Pt present on the anode after testing is the migration of Pt from the Pt/C cathode catalyst layer during cell operation and subsequent deposition onto the anode catalyst layer. The Pt migration may be attributed to the movement of Pt(OH)$_2$ (ref. 67 and 68) or Pt(OH)$_4$$^{2-}$ species, following the electroosmotic flow of OH$^-$ from cathode to anode in accordance with Pourbaix diagram.[69,70] This is in line with significantly decreased ECSA and increased resistance of the Pt/C cathode after 500 h (ESI Fig. 8A and B†). The CeO$_2$ surface provides an anchoring point for the dissolved Pt ions that are reduced under the H$_2$ atmosphere. The concentration of each element was estimated using EDX where values are calculated by taking the average of six

zones for each sample. An examination of the cathode after testing shows that the Pt content drops from 33(7) to 7(2) wt% (sd) on the cathode surface and increases from 0 to 12(4) wt% on the anode surface. The elemental map for F after the durability test also exhibits a negligible change (Fig. 5B).

We also examined the cathode surfaces before and after the 500 h test. The cathode shown in Fig. 6A before testing shows a rather non-homogeneous morphology with zones corresponding to isolated Pt/C catalyst and F-containing ionomer particles. After the 500 h test, the electrode surface remains similar, with portions associated with the Pt/C catalyst particles (Fig. 6B). The significant change is that of the surface concentration of Pt, which drops significantly as described above. The elemental maps for F and C after the durability test indicate a noticeable visible difference (Fig. 6B). Furthermore, the C : F ratio drops dramatically at the cathode after durability testing from 173 : 1 to 4.6 : 1 as quantified by EDX, supporting the hypothesis that ionomer degradation from the anode does not greatly affect the cell durability, but rather carbon corrosion which affects the ionomer content as well, as confirmed by our model as the carbon support is lost with time.

A minor quantity of Pd is also discovered (Fig. 6B), indicating a small amount of reverse migration of Pd across the membrane during operation, although not to the extreme as the Pt migration from cathode to anode. This reverse migration of Pd across the membrane during operation, could either be due to the process of dissolved Pd^{2+} cationic species formed at the anode migrating through AEMs similar to the phenomenon described in some reports discussing anions transporting through Nafion membranes.[71,72] Also, given the high pH, Pd cations can potentially form Pd(OH)$_2$,[73] however we believe this is maybe a gradual concentration polarization process as they move from the anode to the cathode *via* the AEM. Samples of the Pt/C catalyst powder were recovered from the MEAs before
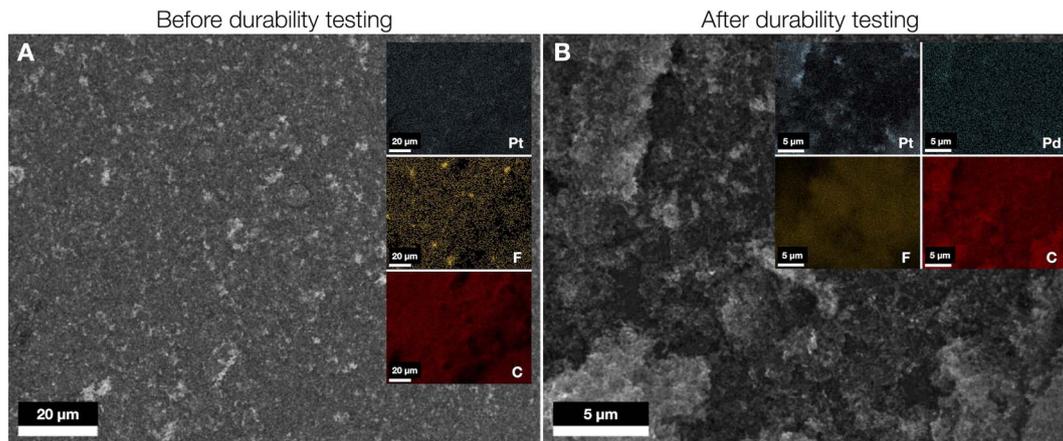
Fig. 6 SEM images and corresponding elemental maps for C, Pt, and F of representative areas of the Pt/C cathode surface. (A) Before testing SEM image and elemental maps for Pt, F and C. (B) After the 500 h durability AEMFC test SEM image and elemental maps for Pt, Pd, F and C. The scale bar setting of all images in (A) is 20 μm and 5 μm for all images in (B).

and after the cell test and analyzed by TEM as shown in ESI Fig. 13.† Clear evidence of Pt corrosion and Ostwald ripening on the "used" catalyst surface can be seen in ESI Fig. 13(C and D)† compared to the fresh catalyst shown in ESI Fig. 13(A and B).† The TEM images of the cathode sample after durability testing show some agglomeration of the remaining Pt particles (ESI Fig. 13(C and D)†). This can help to further explain the mass-transport losses after the shutdown and restart cycle (Fig. 3C).

3.4 Metal nanoparticle detachment and migration from carbonaceous supports in alkaline systems

In alkaline environments, the exact mechanisms of detachment of metal nanoparticles from carbonaceous supports are not deeply understood at the AEMFC device level.[38] However, a few recent investigations have proposed some hypotheses. For instance, Xie and Kirk recently demonstrated poor Pt stability at the cathode of AEMFCs.[67] A Pt/C cathode was held at 0.9 V steady-state potential for 1500 h at 60 °C in an AEMFC test. Significant Pt degradation was observed through dissolution and agglomeration (Ostwald ripening) on the carbon substrate, forming large Pt clusters and Pt also migrated into the polymer membrane structure. This study ran at a very low current density of 3 μA cm^{-2} (simulating OCV conditions) and yet showed significant degradation. Such degradation mechanisms are accelerated in the test reported here, which occurred under much more harsh conditions (600 mA cm^{-2}, high gas flow, 70 °C) and resulted in Pt migration through the membrane and onto the anode. Such a process is aided by the flow of hydrated OH$^-$ ions that pass from the cathode and anode.[74,75] Cross-sectional microscopy of the MEAs could give further insight and help clarify the form in which Pt is present within the AEM and the homogeneity of Pt deposits as shown by Guilminot et al. in PEMFC systems.[76]

The extreme instability of Pt/C in alkaline media has been documented by Chatenet and co-workers using identical location-transmission electron microscopy (IL-TEM) studies which demonstrated that under potential cycling 60% of ECSA

loss after only 150 cycles between 0.1 and 1.23 V vs. RHE. Around 63% of Pt NPs were found to have detached from the carbon surface during the electrochemical treatment. The same authors showed how Pt NP detachment arises from the PGM metal catalyzed (Pt, PtRu, Pd) oxidation of the carbon support to carbonates[77] although this process is less likely to occur in AEMFCs if the intervals between shutdown and restart are short (<30 min). In these scenarios, the membrane–electrode interface remains relatively "dry" giving rise to a situation wherein Pt corrosion and Ostwald ripening are more likely to occur.[78]

Given that the intervals between shutdowns and restarts for automobiles are longer than 30 min on average, we propose a potential mechanism for the detachment of the Pt nano-particles from the carbon support of the cathode of our Pd/C–CeO$_2$-based anode AEMFC. As shown in Fig. 7A, under normal operation, the HOR and ORR electrochemical reactions occur simultaneously on their respective electrodes. However, as shown in Fig. 7B, during a shutdown event the H$_2$ and air gas flows stop, and atmospheric air seeps into the anode and cathode compartments.[79,80] The described mechanism is similar to the reverse-current decay that is well discussed in PEMFC systems.[81–86] After restarting the system and flowing H$_2$, unwanted O$_2$ from the atmospheric air remaining in the anode creates zones of H$_2$ and O$_2$ within the anode. Prior to the shutdown, our AEMFC was fully humidified and after the shutdown, the cell temperature cooled to room temperature faster than the humidifiers. Therefore, excessive water remaining in the anode due to flooding could further decrease the distribution of H$_2$ within the anode. In this transient state, the HOR occurs normally at the anode, but the produced electrons from the reaction can encounter the humidified O$_2$-rich zones of the anode and trigger unavoidable ORR at the anode. Consequentially, the potential at the cathode where ORR normally occurs, jumps to values >1.4 V.[80,87–89] As a result of reverse-current decay, this increased potential in the cathode catalyst layer accelerates the deterioration of the cathode catalyst support, causes agglomeration, and eventually leads to nano-particle detachment and ECSA loss.[38,87,90,91]

10444 | J. Mater. Chem. A, 2024, **12**, 10435–10448

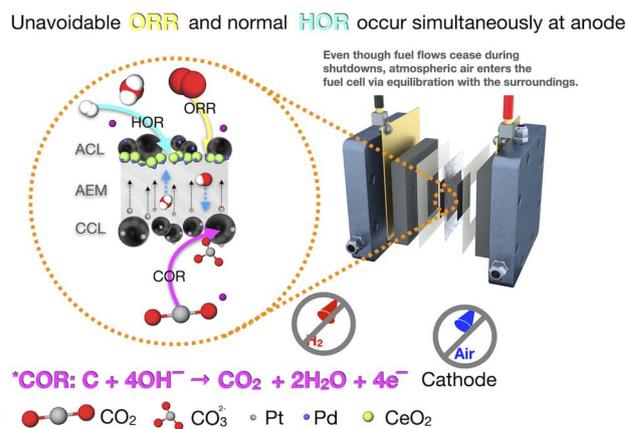This journal is © The Royal Society of Chemistry 2024

Fig. 7 Scheme depicting the electrochemical processes in an AEMFC that occur during; (A) normal operation with H_2 and air flowing through the anode and cathode, respectively. In this case, the hydrogen oxidation reaction (HOR) and oxygen reduction reaction (ORR) occur simultaneously. (B) A shutdown/restart cycle where the H_2 and air flows cease. During periods of dormancy, oxygen from atmospheric air enters the anode compartment due to equilibration with the surroundings. After the system restarts, the residual O_2 in the anode causes unavoidable ORR to occur simultaneously with the normal HOR reaction at the anode. This dual reaction anode phenomenon triggers a high potential at the cathode of >1.4 V, in turn causing a carbon oxidation reaction (COR) to occur at the cathode. The (*) in (B) indicates a further reaction where carbonate ion species are produced ($CO_2 + 2OH^- \rightarrow CO_3^{2-} + H_2O$). ACL and CCL stand for anode catalyst layer and cathode catalyst layer, respectively, in both (A) and (B).

Although the likelihood of this process occurring increases with longer durations of downtime between shutdowns and restarts, we do not know how much it affects carbon corrosion in our work. Existing literature in the PEMFC field suggests that sequences of startup and shutdowns are more detrimental than a single instance; thus, we share this information to encourage the larger AEMFC community to pursue durability studies with startup and shutdown cycles that are more akin to real-world operation and will provide invaluable information to the field.

4. Conclusions

After confirming the robust polarization performance of two Pt-free Pd-based anode AEMFCs, we processed them for an additional 500 h in H_2–air at a high current density of 600 mA cm^{-2} to investigate the degradation mechanisms affecting their long-term durability. Although the events occurred at different periods (@~200 h for the Pd/C–CeO$_2$ anode cell and ~384 h for the Pd/C anode cell), both cells demonstrated eventual declines in performance.

AEMFC studies allude to the fact that higher cell temperatures could potentially increase cell durability since the Pd/C–CeO$_2$ anode cell tested at 70 °C had a lower degradation rate than the cell tested at 60 °C (30 compared to 80 µV h^{-1}) over the same approximate timeframe. Additionally, the chemical degradation of the ionomer in the cathode catalyst layer and the cathode side of the membrane are more deleterious to the cell than that of the anode. These effects can be accounted for by the excess water production at the anode which keeps the ionomer and membrane on the anode side well-hydrated compared to a faster rate of drying of the cathode as shown by 1D modelling. Furthermore, the higher temperature increases the reaction

kinetics, and more water is transported to the cathode side keeping it hydrated, lessening the degradation rate.

Changes in the original cathode ECSA value by as much as 48% for the Pd/C–CeO$_2$ anode cells revealed that dissolution of Pt particles due to oxidation of the carbon support was another culprit for performance degradation. The shutdown/restart event exacerbated the Pt detachment as confirmed by *ex situ* microscopy which showed Pt particles from the cathode redeposited onto the CeO$_2$ and carbon surfaces of the anode after apparent migration through the AEM. Although to a significantly lower extent, reverse migration of Pd from the anode to the cathode occurred as well indicating that the anode catalyst layer was much more robust and provided higher resistance to nanoparticle detachment.

At more extreme conditions such as higher current densities, flow rates, and temperatures these degradation mechanisms are projected to compound and further limit the cell's life. While this work presents a significant landmark for degradation mechanisms in AEMFCs with Pt-free anodes, it is also meant to inspire mitigation strategies such as the design of metal-carbon support catalysts with stronger binding layers between the metal NPs and carbon supports or carbon-free support NP catalysts that exhibit high activity while simultaneously allaying durability issues associated with shutdown/restart operation cycles in alkaline environments for the next generation of highly durable AEMFCs.

Data availability

Source data for the main text figures are available through figshare.com: **https://doi.org/10.6084/m9.figshare.24226012**.

Author contributions

Conceptualization by J. C. D., R. K. S., B. S. P., D. R. D.; data curation and visualization by J. C. D., R. K. S., A. C. Y.-N., C. H., H. A. M., M. V. P., L. C., E. C.-A.; formal analysis and validation by J. C. D., R. K. S., A. C. Y.-N., C. H., K. Y., H. A. M., M. V. P., L. C., E. C.-A., P. J. F.; funding acquisition by H. A. M., S. B., P. J. F., B. S. P., D. R. D.; investigation by J. C. D., R. K. S., A. C. Y.-N., C. H., K. Y., M. V. P., L. C., E. C.-A., P. J. F.; methodology by S. B., P. J. F., B. S. P., D. R. D.; project administration, resources and supervision by S. B., P. J. F., B. S. P., D. R. D.; software by S. B., D. R. D.; writing – original draft by J. C. D., R. K. S.; writing – review & editing by J. C. D., R. K. S., A. C. Y.-N., C. H., K. Y., H. A. M, M. V. P., L. C., E. C.-A., S. B., P. J. F., B. S. P., D. R. D.

Conflicts of interest

There are no conflicts to declare.

Acknowledgements

References

1 I. Staffell, D. Scamman, A. Velazquez Abad, P. Balcombe, P. E. Dodds, P. Ekins, N. Shah and K. R. Ward, *Energy Environ. Sci.*, 2019, **12**, 463–491.

2 Z. P. Cano, D. Banham, S. Ye, A. Hintennach, J. Lu, M. Fowler and Z. Chen, *Nat. Energy*, 2018, **3**, 279–289.

3 M. K. Debe, *Nature*, 2012, **486**, 43–51.

4 B. Pivovar, *Nat. Catal.*, 2019, **2**, 562–565.

5 C. B. Corporation, Canada's first hydrogen train is taking passengers, https://www.cbc.ca/news/science/hydrogen-train-quebec-city-1.6888891, accessed 22-08-23.

6 J. Post, Israel launches first hydrogen fuel station: Start of energy market revolution?, https://www.jpost.com/business-and-innovation/energy-and-infrastructure/article-742546, accessed 22-08-23.

7 B. P. Setzler, Z. Zhuang, J. A. Wittkopf and Y. Yan, *Nat. Nanotechnol.*, 2016, **11**, 1020–1025.

8 X. X. Wang, M. T. Swihart and G. Wu, *Nat. Catal.*, 2019, **2**, 578–589.

9 R. Abbasi, B. P. Setzler and Y. Yan, *Energy Environ. Sci.*, 2023, **16**, 4404–4422.

10 D. R. Dekel, *ECS Trans.*, 2013, **50**, 2051–2052.

11 M. M. Hossen, M. S. Hasan, M. R. I. Sardar, J. b. Haider, M. Mottakin, K. Tammeveski and P. Atanassov, *Appl. Catal., B*, 2023, **325**, 121733.

12 A. Sarapuu, J. Lilloja, S. Akula, J. H. Zagal, S. Specchia and K. Tammeveski, *ChemCatChem*, 2023, **15**(22), e202300849.

13 N. Chen, H. H. Wang, S. P. Kim, H. M. Kim, W. H. Lee, C. Hu, J. Y. Bae, E. S. Sim, Y.-C. Chung, J.-H. Jang, S. J. Yoo, Y. Zhuang and Y. M. Lee, *Nat. Commun.*, 2021, **12**(1), 2367.

14 G. Huang, M. Mandal, X. Peng, A. C. Yang-Neyerlin, B. S. Pivovar, W. E. Mustain and P. A. Kohl, *J. Electrochem. Soc.*, 2019, **166**, F637–F644.

15 J. Pan, C. Chen, Y. Li, L. Wang, L. Tan, G. Li, X. Tang, L. Xiao, J. Lu and L. Zhuang, *Energy Environ. Sci.*, 2014, **7**, 354–360.

16 J. Wang, Y. Zhao, B. P. Setzler, S. Rojas-Carbonell, C. Ben Yehuda, A. Amel, M. Page, L. Wang, K. Hu, L. Shi, S. Gottesfeld, B. Xu and Y. Yan, *Nat. Energy*, 2019, **4**, 392–398.

17 L. Wang, X. Peng, W. E. Mustain and J. R. Varcoe, *Energy Environ. Sci.*, 2019, **12**, 1575–1579.

18 J. R. Varcoe, P. Atanassov, D. R. Dekel, A. M. Herring, M. A. Hickner, P. A. Kohl, A. R. Kucernak, W. E. Mustain, K. Nijmeijer, K. Scott, T. Xu and L. Zhuang, *Energy Environ. Sci.*, 2014, **7**, 3135–3191.

19 Z. Huang, R. Lu, Y. Zhang, W. Chen, G. Chen, C. Ma, Z. Wang, Y. Han and W. Huang, *Adv. Funct. Mater.*, 2023, **33**(47), 2306333.

20 L. Han, P. Ou, W. Liu, X. Wang, H.-T. Wang, R. Zhang, C.-W. Pao, X. Liu, W.-F. Pong, J. Song, Z. Zhuang, M. V. Mirkin, J. Luo and H. L. Xin, *Sci. Adv.*, 2022, **8**(22), eabm3779.

21 Q. Sun, N. J. Oliveira, S. Kwon, S. Tyukhtenko, J. J. Guo, N. Myrthil, S. A. Lopez, I. Kendrick, S. Mukerjee, L. Ma, S. N. Ehrlich, J. Li, W. A. Goddard, Y. Yan and Q. Jia, *Nat. Energy*, 2023, **8**, 859–869.

22 F.-Y. Gao, S.-N. Liu, J.-C. Ge, X.-L. Zhang, L. Zhu, Y.-R. Zheng, Y. Duan, S. Qin, W. Dong, X. Yu, R.-C. Bao, P.-P. Yang, Z.-Z. Niu, Z.-G. Ding, W. Liu, S. Lan, M.-R. Gao, Y. Yan and S.-H. Yu, *Nat. Catal.*, 2022, **5**, 993–1005.

23 Y. Wang, G. Wang, G. Li, B. Huang, J. Pan, Q. Liu, J. Han, L. Xiao, J. Lu and L. Zhuang, *Energy Environ. Sci.*, 2015, **8**, 177–181.

24 Y. Zhou, Z. Xie, J. Jiang, J. Wang, X. Song, Q. He, W. Ding and Z. Wei, *Nat. Catal.*, 2020, **3**, 454–462.

25 Y. Xue, L. Shi, X. Liu, J. Fang, X. Wang, B. P. Setzler, W. Zhu, Y. Yan and Z. Zhuang, *Nat. Commun.*, 2020, **11**(1), 5651.

26 H. A. Miller, A. Lavacchi, F. Vizza, M. Marelli, F. Di Benedetto, F. D'Acapito, Y. Paska, M. Page and D. R. Dekel, *Angew. Chem., Int. Ed.*, 2016, **55**, 6004–6007.

27 R. K. Singh, E. S. Davydova, J. Douglin, A. O. Godoy, H. Tan, M. Bellini, B. J. Allen, J. Jankovic, H. A. Miller,

10446 | *J. Mater. Chem. A*, 2024, **12**, 10435–10448

This journal is © The Royal Society of Chemistry 2024

A. C. Alba-Rubio and D. R. Dekel, *Adv. Funct. Mater.*, 2020, **30**(38), 2002087.

28 E. R. Hamo, R. K. Singh, J. C. Douglin, S. Chen, M. B. Hassine, E. Carbo-Argibay, S. Lu, H. Wang, P. J. Ferreira, B. A. Rosen and D. R. Dekel, *ACS Catal.*, 2021, **11**, 932–947.

29 M. V. Pagliaro, C. Wen, B. Sa, B. Liu, M. Bellini, F. Bartoli, S. Sahoo, R. K. Singh, S. P. Alpay, H. A. Miller and D. R. Dekel, *ACS Catal.*, 2022, **12**, 10894–10904.

30 N. Ul Hassan, M. Mandal, G. Huang, H. A. Firouzjaie, P. A. Kohl and W. E. Mustain, *Adv. Energy Mater.*, 2020, **10**.

31 X. Peng, D. Kulkarni, Y. Huang, T. J. Omasta, B. Ng, Y. Zheng, L. Wang, J. M. LaManna, D. S. Hussey, J. R. Varcoe, I. V. Zenyuk and W. E. Mustain, *Nat. Commun.*, 2020, **11**(1), 3561.

32 T. J. Omasta, A. M. Park, J. M. LaManna, Y. Zhang, X. Peng, L. Wang, D. L. Jacobson, J. R. Varcoe, D. S. Hussey, B. S. Pivovar and W. E. Mustain, *Energy Environ. Sci.*, 2018, **11**, 551–558.

33 J. C. Douglin, J. A. Zamora Zeledón, M. E. Kreider, R. K. Singh, M. B. Stevens, T. F. Jaramillo and D. R. Dekel, *Nat. Energy*, 2023, **8**(11), 1262–1272.

34 Y. Wang, Y. Yang, S. Jia, X. Wang, K. Lyu, Y. Peng, H. Zheng, X. Wei, H. Ren, L. Xiao, J. Wang, D. A. Muller, H. D. Abruña, B. J. Hwang, J. Lu and L. Zhuang, *Nat. Commun.*, 2019, **10**(1), 1506.

35 N. Zion, J. C. Douglin, D. A. Cullen, P. Zelenay, D. R. Dekel and L. Elbaz, *Adv. Funct. Mater.*, 2021, **31**(24), 2100963.

36 H. Adabi, A. Shakouri, N. Ul Hassan, J. R. Varcoe, B. Zulevi, A. Serov, J. R. Regalbuto and W. E. Mustain, *Nat. Energy*, 2021, **6**, 834–843.

37 J. Fan, S. Willdorf-Cohen, E. M. Schibli, Z. Paula, W. Li, T. J. G. Skalski, A. T. Sergeenko, A. Hohenadel, B. J. Frisken, E. Magliocca, W. E. Mustain, C. E. Diesendruck, D. R. Dekel and S. Holdcroft, *Nat. Commun.*, 2019, **10**(1), 2306.

38 W. E. Mustain, M. Chatenet, M. Page and Y. S. Kim, *Energy Environ. Sci.*, 2020, **13**, 2805–2838.

39 T. J. Omasta, X. Peng, H. A. Miller, F. Vizza, L. Wang, J. R. Varcoe, D. R. Dekel and W. E. Mustain, *J. Electrochem. Soc.*, 2018, **165**, J3039–J3044.

40 N. Ul Hassan, M. J. Zachman, M. Mandal, H. Adabi Firouzjaie, P. A. Kohl, D. A. Cullen and W. E. Mustain, *ACS Catal.*, 2022, **12**, 8116–8126.

41 H. Peng, Q. Li, M. Hu, L. Xiao, J. Lu and L. Zhuang, *J. Power Sources*, 2018, **390**, 165–167.

42 M. Mandal, G. Huang, N. U. Hassan, X. Peng, T. Gu, A. H. Brooks-Starks, B. Bahar, W. E. Mustain and P. A. Kohl, *J. Electrochem. Soc.*, 2019, **167**(5), 054501.

43 E. S. Davydova, F. D. Speck, M. T. Y. Paul, D. R. Dekel and S. Cherevko, *ACS Catal.*, 2019, **9**, 6837–6845.

44 E. S. Davydova, S. Mukerjee, F. Jaouen and D. R. Dekel, *ACS Catal.*, 2018, **8**, 6665–6690.

45 H. A. Miller, F. Vizza, M. Marelli, A. Zadick, L. Dubau, M. Chatenet, S. Geiger, S. Cherevko, H. Doan, R. K. Pavlicek, S. Mukerjee and D. R. Dekel, *Nano Energy*, 2017, **33**, 293–305.

46 H. Yu, E. S. Davydova, U. Ash, H. A. Miller, L. Bonville, D. R. Dekel and R. Maric, *Nano Energy*, 2019, **57**, 820–826.

47 D. Strmcnik, M. Uchimura, C. Wang, R. Subbaraman, N. Danilovic, D. van der Vliet, A. P. Paulikas, V. R. Stamenkovic and N. M. Markovic, *Nat. Chem.*, 2013, **5**, 300–306.

48 J. Li, S. Ghoshal, M. K. Bates, T. E. Miller, V. Davies, E. Stavitski, K. Attenkofer, S. Mukerjee, Z.-F. Ma and Q. Jia, *Angew. Chem., Int. Ed.*, 2017, **56**, 15594–15598.

49 F. D. Speck, F. S. M. Ali, M. T. Y. Paul, R. K. Singh, T. Böhm, A. Hofer, O. Kasian, S. Thiele, J. Bachmann, D. R. Dekel, T. Kallio and S. Cherevko, *Chem. Mater.*, 2020, **32**, 7716–7724.

50 A. C. Yang-Neyerlin, C. He, S. Medina, S. Pylypenko and B. S. Pivovar, *ECS Meet. Abstr.*, 2021, **MA2021-02**, 1218.

51 A. G. Divekar, M. C. Kuo, A. M. Park, A. R. Motz, Z. S. Page-Belknap, Z. Owczarczyk, H. Long, S. Seifert, C. M. Maupin, M. A. Yandrasits, Y. Yang, B. S. Pivovar and A. M. Herring, *J. Polym. Sci., Part B: Polym. Phys.*, 2019, **57**, 700–712.

52 J. C. Douglin, J. R. Varcoe and D. R. Dekel, *J. Power Sources Adv.*, 2020, **5**, 100023.

53 J. C. Douglin, R. K. Singh, A. C. Yang-Neyerlin, C. He, K. Yassin, H. A. Miller, M. V. Pagliaro, L. Capozzoli, E. Carbo-Argibay, S. Brandon, P. J. Ferreira, B. Pivovar and D. R. Dekel, *J. Mater. Chem. A*, 2024, DOI: 10.6084/m9.figshare.24226012.

54 D. R. Dekel, I. G. Rasin and S. Brandon, *J. Power Sources*, 2019, **420**, 118–123.

55 K. Yassin, J. C. Douglin, I. G. Rasin, P. G. Santori, B. Eriksson, N. Bibent, F. Jaouen, S. Brandon and D. R. Dekel, *Energy Convers. Manage.*, 2022, **270**, 116203.

56 S. T. Thompson, D. Peterson, D. Ho and D. Papageorgopoulos, *J. Electrochem. Soc.*, 2020, **167**(8), 084514.

57 B. Eriksson, P. G. Santori, F. Lecoeur, M. Dupont and F. Jaouen, *J. Power Sources*, 2023, **554**, 232343.

58 T. J. Omasta, L. Wang, X. Peng, C. A. Lewis, J. R. Varcoe and W. E. Mustain, *J. Power Sources*, 2018, **375**, 205–213.

59 Z. A. Feng, F. El Gabaly, X. Ye, Z.-X. Shen and W. C. Chueh, *Nat. Commun.*, 2014, **5**(1), 4374.

60 K. Yassin, I. G. Rasin, S. Willdorf-Cohen, C. E. Diesendruck, S. Brandon and D. R. Dekel, *J. Power Sources Adv.*, 2021, **11**, 100066.

61 H. A. Gasteiger, J. E. Panels and S. G. Yan, *J. Power Sources*, 2004, **127**, 162–171.

62 B. P. Setzler and T. F. Fuller, *J. Electrochem. Soc.*, 2015, **162**, F519–F530.

63 M. Ciureanu, H. Wang and Z. Qi, *J. Phys. Chem. B*, 1999, **103**, 9645–9657.

64 R. K. Singh, R. Devivaraprasad, T. Kar, A. Chakraborty and M. Neergat, *J. Electrochem. Soc.*, 2015, **162**, F489–F498.

65 R. Makharia, M. F. Mathias and D. R. Baker, *J. Electrochem. Soc.*, 2005, **152**(5), A970.

66 M. Bellini, M. V. Pagliaro, A. Lenarda, P. Fornasiero, M. Marelli, C. Evangelisti, M. Innocenti, Q. Jia, S. Mukerjee, J. Jankovic, L. Wang, J. R. Varcoe,

This journal is © The Royal Society of Chemistry 2024

J. Mater. Chem. A, 2024, **12**, 10435–10448 | **10447**

C. B. Krishnamurthy, I. Grinberg, E. Davydova, D. R. Dekel, H. A. Miller and F. Vizza, *ACS Appl. Energy Mater.*, 2019, **2**, 4999–5008.

67 L. Xie and D. W. Kirk, *Electrocatalysis*, 2020, **11**, 292–300.

68 A. Raut, H. Fang, Y. C. Lin, S. Fu, D. Sprouster, R. Shimogawa, A. I. Frenkel, C. Bae, J. C. Douglin, J. Lillojad, K. Tammeveski, Z. Zeng, S. Bliznakov, M. Rafailovich and D. R. Dekel, *Angew. Chem., Int. Ed.*, 2023, **62**(37), e202306754.

69 M. Pourbaix, *Atlas of Electrochemical Equilibria in Aqueous Solutions*, NACE, 1966.

70 R. Granados-Fernández, M. A. Montiel, S. Díaz-Abad, M. A. Rodrigo and J. Lobato, *Catalysts*, 2021, **11**.

71 V. Freger, *Adv. Colloid Interface Sci.*, 2020, **277**, 102107.

72 Y. S. Oren, O. Nir and V. Freger, *J. Membr. Sci.*, 2024, **690**, 122202.

73 G. Montegrossi, A. Giaccherini, E. Berretti, F. D. Benedetto, M. Innocenti, F. d'Acapito and A. Lavacchi, *J. Electrochem. Soc.*, 2017, **164**, E3690–E3695.

74 M. Schalenbach, O. Kasian, M. Ledendecker, F. D. Speck, A. M. Mingers, K. J. J. Mayrhofer and S. Cherevko, *Electrocatalysis*, 2017, **9**, 153–161.

75 A. Zadick, L. Dubau, N. Sergent, G. Berthomé and M. Chatenet, *ACS Catal.*, 2015, **5**, 4819–4824.

76 E. Guilminot, A. Corcella, F. Charlot, F. Maillard and M. Chatenet, *J. Electrochem. Soc.*, 2007, **154**(1), B96.

77 C. Lafforgue, F. Maillard, V. Martin, L. Dubau and M. Chatenet, *ACS Catal.*, 2019, **9**, 5613–5622.

78 C. Lafforgue, M. Chatenet, L. Dubau and D. R. Dekel, *ACS Catal.*, 2018, **8**, 1278–1286.

79 C. A. Reiser, L. Bregoli, T. W. Patterson, J. S. Yi, J. D. Yang, M. L. Perry and T. D. Jarvi, *Electrochem. Solid-State Lett.*, 2005, **8**(6), A273.

80 S.-M. Jung, S.-W. Yun, J.-H. Kim, S.-H. You, J. Park, S. Lee, S. H. Chang, S. C. Chae, S. H. Joo, Y. Jung, J. Lee, J. Son, J. Snyder, V. Stamenkovic, N. M. Markovic and Y.-T. Kim, *Nat. Catal.*, 2020, **3**, 639–648.

81 M. F. Mathias, R. Makharia, H. A. Gasteiger, J. J. Conley, T. Fuller, C. Gittleman and S. S. Kocha, *Electrochem. Soc. Interface.*, 2005, **14**, 24–35.

82 M. Oszcipok, M. Zedda, D. Riemann and D. Geckeler, *J. Power Sources*, 2006, **154**, 404–411.

83 T. F. Fuller and J. Newman, *J. Electrochem. Soc.*, 2019, **140**, 1218–1225.

84 L. M. Roen, C. H. Paik and T. D. Jarvi, *Electrochem. Solid-State Lett.*, 2004, **7**(1), A19.

85 R. Borup, J. Meyers, B. Pivovar, Y. S. Kim, R. Mukundan, N. Garland, D. Myers, M. Wilson, F. Garzon, D. Wood, P. Zelenay, K. More, K. Stroh, T. Zawodzinski, J. Boncella, J. E. McGrath, M. Inaba, K. Miyatake, M. Hori, K. Ota, Z. Ogumi, S. Miyata, A. Nishikata, Z. Siroma, Y. Uchimoto, K. Yasuda, K.-i. Kimijima and N. Iwashita, *Chem. Rev.*, 2007, **107**, 3904–3951.

86 T. W. Patterson and R. M. Darling, *Electrochem. Solid-State Lett.*, 2006, **9**(4), A183.

87 N. Staud and P. N. Ross, *J. Electrochem. Soc.*, 1986, **133**, 1079–1084.

88 S. Möller, S. Barwe, J. Masa, D. Wintrich, S. Seisel, H. Baltruschat and W. Schuhmann, *Angew. Chem., Int. Ed.*, 2019, **59**, 1585–1589.

89 N. Yousfi-Steiner, P. Moçotéguy, D. Candusso and D. Hissel, *J. Power Sources*, 2009, **194**, 130–145.

90 C. Lafforgue, A. Zadick, L. Dubau, F. Maillard and M. Chatenet, *Fuel Cells*, 2018, **18**, 229–238.

91 R. B. Kaspar, J. A. Wittkopf, M. D. Woodroof, M. J. Armstrong and Y. Yan, *J. Electrochem. Soc.*, 2016, **163**, F377–F383.

10448 | *J. Mater. Chem. A*, 2024, **12**, 10435–10448

This journal is © The Royal Society of Chemistry 2024